

OBSERVATIONS OF THE CRAB NEBULA AND ITS PULSAR IN THE FAR-ULTRAVIOLET AND IN THE OPTICAL^{1,2}

JESPER SOLLERMAN,^{3,4,5} PETER LUNDQVIST,³ DON LINDLER,⁶ ROGER A. CHEVALIER,⁷ CLAES FRANSSON,³
 THEODORE R. GULL,⁶ CHUN S. J. PUN,⁶ AND GEORGE SONNEBORN⁶

Received 1999 October 14; accepted 2000 February 2

ABSTRACT

We present far-UV observations of the Crab Nebula and its pulsar made with the Space Telescope Imaging Spectrograph on board the *Hubble Space Telescope*. Broad, blueshifted absorption arising in the nebula is seen in C IV $\lambda 1550$, reaching a blueward velocity of $\sim 2500 \text{ km s}^{-1}$. This can be interpreted as evidence for a fast outer shell surrounding the Crab Nebula, and we adopt a spherically symmetric model to constrain the properties of such a shell. From the line profile we find that the density appears to decrease outward in the shell. A likely lower limit to the shell mass is $\sim 0.3 M_{\odot}$ with an accompanying kinetic energy of $\sim 1.5 \times 10^{49}$ ergs. A fast massive shell with 10^{51} ergs cannot be excluded but is less likely if the density profile is much steeper than $\rho(R) \propto R^{-4}$ and the maximum velocity is $\lesssim 6000 \text{ km s}^{-1}$. The observations cover the region 1140–1720 Å, which is further into the ultraviolet than has previously been obtained for the pulsar. With the time-tag mode of the spectrograph we obtain the pulse profile in this spectral regime. The profile is similar to that previously obtained by us in the near-UV, although the primary peak is marginally narrower. Together with the near-UV data, and new optical data from the Nordic Optical Telescope, our spectrum of the Crab pulsar covers the entire region from 1140 to 9250 Å. Dereddening the spectrum with a standard extinction curve we achieve a flat spectrum for the reddening parameters $E(B-V) = 0.52$, $R = 3.1$. This dereddened spectrum of the Crab pulsar can be fitted by a power law with spectral index $\alpha_v = 0.11 \pm 0.04$. The main uncertainty in determining the spectral index is the amount and characteristics of the interstellar reddening, and we have investigated the dependence of α_v on $E(B-V)$ and R . In the extended emission covered by our $25'' \times 0.5$ slit in the far-UV, we detect C IV $\lambda 1550$ and He II $\lambda 1640$ emission lines from the Crab Nebula. Several interstellar absorption lines are detected along the line of sight to the pulsar. The Ly α absorption indicates a column density of $(3.0 \pm 0.5) \times 10^{21} \text{ cm}^{-2}$ of neutral hydrogen, which agrees well with our estimate of $E(B-V) = 0.52$ mag. Other lines show no evidence of severe depletion of metals in atomic gas.

Subject headings: dust, extinction — instrumentation: spectrographs —
 pulsars: individual (Crab Pulsar) — supernova remnants — ultraviolet: ISM —
 ultraviolet: stars

1. INTRODUCTION

The Crab Nebula and its pulsar (PSR 0531+21) are among the most studied objects in the sky. The discovery of the Crab pulsar as a fast-rotating radio pulsar (Staelin & Reifenstein 1968; Comella et al. 1969) paved the way for the interpretation of pulsars as neutron stars (Gold 1968). Also, the position of the Crab pulsar in the center of the Crab Nebula, which is the remnant of SN 1054, clearly supports the supernova–neutron star connection. Soon after the radio detection the pulsar was also shown to emit optical pulsations (Cocke, Disney, & Taylor 1969). This established that the pulsating star was the well-known south-preceding star in the center of the nebula, which early optical spectroscopy showed to emit a featureless continuum (Minkowski

1942). To date, more than 1000 radio pulsars are known, but only the following few have optical counterparts known to pulsate also in visible light: the Crab pulsar (Cocke et al. 1969), the LMC pulsar 0540–69 (Middleditch & Pennybaker 1985), the Vela pulsar (Wallace et al. 1977), PSR 0656+14 (Shearer et al. 1997), and (possibly) the Geminga pulsar (Shearer et al. 1998). In the near-UV (NUV), pulsations have been established only for the Crab pulsar (Percival et al. 1993; Gull et al. 1998, hereafter G98). Owing to the faintness of these objects in the optical and in the ultraviolet, the spectroscopic information is very limited. PSR 0540–69 was observed with the Faint Object Spectrograph (FOS) on board *Hubble Space Telescope* (HST) in the 2500–5000 Å range (Hill et al. 1997) and showed a rather steep power-law spectrum. These observations were, however, contaminated by nebular emission. The Geminga pulsar was observed with the Keck telescope (Martin, Halpern, & Schiminovich 1998), but the spectrum has very low signal-to-noise ratio because this pulsar is exceedingly faint in the optical. The only pulsar for which good signal-to-noise ratio spectroscopy in the optical and ultraviolet can be obtained is the Crab pulsar. Surprisingly enough, very little has been done in this respect since the optical observations of Oke (1969). In particular, until the study by G98, no UV spectroscopy of the Crab pulsar had been published since the first attempts by the *International Ultraviolet Explorer* (IUE) (Benvenuti et al. 1980). The IUE data

¹ Based on observations with the NASA/ESA *Hubble Space Telescope*, obtained at the Space Telescope Science Institute, which is operated by the Association of Universities for Research in Astronomy, Inc. under NASA contract NAS5-26555.

² Based on observations obtained at the *Nordic Optical Telescope* on La Palma, using the Andalucia Focal Reducer and Spectrograph.

³ Stockholm Observatory, SE-133 36 Saltsjöbaden, Sweden.

⁴ European Southern Observatory, Karl-Schwarzschild-Strasse 2, D-857 48 Garching, Germany.

⁵ Send offprint requests to Jesper Sollerman; jesper@astro.su.se.

⁶ Goddard Space Flight Center, Code 681, Greenbelt, MD 20771.

⁷ Department of Astronomy, University of Virginia, P.O. Box 3818, Charlottesville, VA 22903.

cover only the NUV region (2000–3150 Å) and have poor signal-to-noise ratio. The *HST*/STIS (Space Telescope Imaging Spectrograph) data from G98, and the new data presented here, clearly supersede these early attempts.

The Crab pulsar has been extensively studied over a very broad wavelength range, from the radio up to γ -rays (e.g., Lyne & Graham-Smith 1998). The high-energy emission, from infrared (IR) to γ -rays, is believed to be the result of the same emission mechanism (e.g., Lyne & Graham-Smith 1998). It is therefore of interest to fill in the gaps in the observed spectrum of the pulsar in this range. Although the pulsar is relatively bright in the optical, UV observations are difficult owing to the large extinction toward the Crab, $E(B - V) \sim 0.5$ mag (e.g., Davidson & Fesen 1985, and references therein). Here, we present UV observations of the Crab pulsar further into the far-UV (FUV) (1140–1720 Å) than has previously been obtained. These are presented together with our previous NUV data (1600–3200 Å) (G98) and new optical data from the Nordic Optical Telescope (NOT). Owing to the large extinction correction, great care must be taken to draw conclusions about the intrinsic spectrum and thus the emission mechanism of the pulsar. However, this procedure might also give a hint on the absorption properties of the dust in the direction toward the pulsar.

In addition to the pulsar emission, we detect emission lines from the Crab Nebula itself in the FUV. In particular, the strength of the C IV $\lambda 1550$ emission can be of interest for abundance determinations. Even more interesting is the broad C IV $\lambda 1550$ absorption line from the nebula detected against the pulsar continuum. This line provides information on the nature of the SN 1054 event.

Although the Crab Nebula has been studied extensively, the nature of the progenitor remains unknown. According to models based on the existence of the central neutron star, as well as on nucleosynthesis arguments, the zero-age main-sequence (ZAMS) mass of the progenitor was probably in the range 8–13 M_{\odot} (Nomoto 1985). The amount of material observed in the nebula ($4.6 \pm 1.8 M_{\odot}$) seems too low to account for this (Fesen, Shull, & Hurford 1997). Furthermore, the velocities of the filaments (~ 1400 km s $^{-1}$; Davidson & Fesen 1985) give an uncomfortably low kinetic energy ($\leq 1 \times 10^{50}$ ergs) compared to other supernova remnants, i.e., at least an order of magnitude less than the canonical energy of core-collapse supernovae, 10^{51} ergs.

The “missing mass” could either be in a slow progenitor wind or in a fast, hitherto undetected, shell ejected at the explosion (Chevalier 1977). If the latter is true, as is hinted by the observations of the outer [O III] skin of the nebula (Hester et al. 1996; Sankrit & Hester 1997), this shell might account for the missing mass and kinetic energy of the nebula. The question remains, however, why such a shell has escaped detection despite many efforts to observe it (see, e.g., Fesen et al. 1997). One possibility is that the low density of the surrounding gas is not high enough to give rise to detectable circumstellar emission when interacting with the ejecta; neither X-ray nor radio searches have indicated any evidence of circumstellar interaction between fast ejecta and ambient gas (Mauche & Gorenstein 1989; Frail et al. 1995). If a fast shell is absent, the birth of the Crab was definitely a low-energy event. This would call for a revision of our understanding of supernova explosions, especially since SN 1054 apparently was not unusually dim according to historical records (Chevalier 1977; Wheeler 1978).

It is thus of great interest to investigate further whether there is a stellar wind or supernova ejecta outside the observed nebula and what velocity this gas may have. Lundqvist, Fransson, & Chevalier (1986, hereafter LFC86) proposed to search for a fast shell by looking in the UV toward the Crab pulsar. Their time-dependent photoionization calculations showed that C IV $\lambda 1550$ could show up in blueshifted absorption if the ionization history of the shell was as predicted in some models of Reynolds & Chevalier (1984). Here, we present the detection of this broad absorption line and discuss its implications for the fast shell around the Crab Nebula.

First we discuss the observations and reductions (§ 2). We then (§ 3) discuss the pulse profile, the amount of reddening toward the pulsar, and the intrinsic pulsar spectrum in the optical/UV. In § 3 we also discuss the lines originating from the interstellar gas toward the pulsar and from the Crab Nebula itself. Some of these observations constrain the properties of a possible outer shell. In § 4 we summarize our conclusions.

2. OBSERVATIONS, REDUCTIONS, AND RESULTS

2.1. *HST* Far-UV Observations

The Crab pulsar was observed on 1999 January 22 using *HST*/STIS (Kimble et al. 1998) with the FUV Multi Anode Micro-channel Array (MAMA) detector. The low-resolution grating G140L was used, which covers the wavelength interval 1140–1720 Å. These observations were made in the time-tag mode and used a slit of $52'' \times 0''.5$. The spectral resolution is $0.58 \text{ Å pixel}^{-1}$, and the plate scale is $0''.0244 \text{ pixel}^{-1}$. This means that only $25''$ of the long slit is actually projected onto the detector. In total, six orbits of observations, including target acquisition, were used. These were divided into two visits. A log of the observations is shown in Table 1. The total on-target exposure time amounted to 14,040 s. The orientation of the slit is shown in Figure 1.

2.1.1. Time-resolved Emission

The time-tag mode on the STIS allows us to resolve the emission from the Crab pulsar both in wavelength and time. The time resolution obtained in this mode is 125 μ s. As these observations were the first to utilize the time-tag capabilities of *HST*/STIS in the FUV for a known periodic variable, special software, developed at Goddard Space Flight Center (GSFC), was used to obtain the pulse profile for the pulsar. The analysis followed the procedures outlined in G98. For each of the six data sets, a time-averaged image was produced to trace the position of the pulsar spectrum. A 13 pixel wide window was used to extract events in the pulsar spectrum as well as in the background emission at both sides of the pulsar emission. The arrival time of each

TABLE 1
LOG OF STIS FUV OBSERVATIONS

Observation	Start Time (MJD) (51200.0 +)	Exposure Time (s)
O4ZP01010.....	.54924	2100
O4ZP01020.....	.60619	2460
O4ZP01030.....	.67384	2460
O4ZP01040.....	.74103	2460
O4ZP02010.....	.81802	2100
O4ZP02020.....	.87488	2460

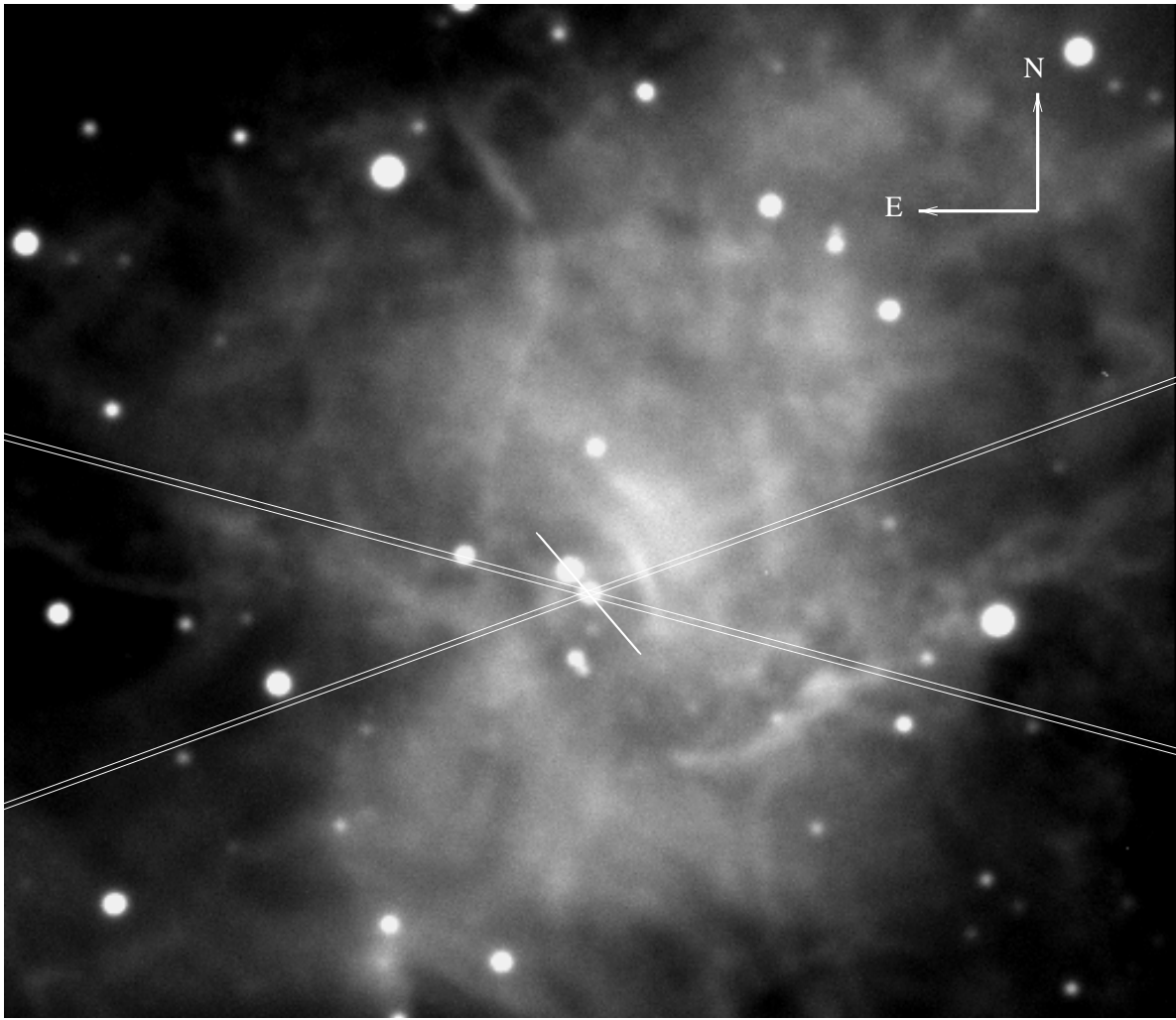


FIG. 1.—R-band image of the Crab Nebula obtained at the NOT in 1998 December. Shown are the extents and position angles of the slits used in the optical and in the FUV. The STIS-FUV slit is $25''$ long. The NUV observation (G98) used a $2'' \times 2''$ aperture centered on the pulsar.

$125 \mu\text{s}$ sample was converted to a solar system barycenter arrival time. The position of the *HST* with respect to earth center was computed by the Flight Dynamics Facility at GSFC with errors less than 200 m. The position of the Earth with respect to the solar system barycenter was computed using a routine, SOLSYS, supplied by the US Naval Observatory (Kaplan et al. 1989). All events in the pulsar spectrum (and in the background regions) were assigned a (barycentric) arrival time with respect to the start of the first exposure. As we found a small drift in the times recorded in the FITS headers, we used the internal clock from the engineering mode header to do this. To determine the period we folded the arrival times modulo a grid of test frequencies, f_i , and corrected for the slowdown rate of the pulsar. Pulse profiles were calculated as histograms of the function $f(t) = f_i t + \dot{f} t^2/2$, where the data were co-added into 512 phase bins. The appropriate value of f_i was then determined by maximizing the sum of squares of the values in the pulse profile.

In this procedure we used a value for \dot{f} from radio observations at Jodrell Bank⁸ (Lyne, Pritchard, & Roberts 1999),

while the second time derivative is unimportant for this purpose. This resulted in a measured period of $P = 33.492675$ ms at Modified Julian Date (MJD) 51200.549, the time of the beginning of our first observation (number O4ZP01010). As the data were obtained during a time period of 8 hr, we could also determine the pulsar slowdown rate from our observations. We obtained $\dot{P} = (4.0 \pm 0.4) \times 10^{-13} \text{ s s}^{-1}$, which is consistent with the value used above from the radio observations, $4.2 \times 10^{-13} \text{ s s}^{-1}$.

In Figure 2 we show the Crab pulsar pulse profile in the FUV regime. It was obtained by subtracting the background from the pulse profile obtained for the period given above. For comparison, the figure also shows the NUV pulse profile from G98.

2.1.2. Phase-averaged Spectrum

Averaging over the pulse we obtain a phase-averaged spectrum of the pulsar that covers the region 1140–1720 Å. This spectrum probes the emission of the Crab pulsar further into the UV than has previously been done and is shown in Figure 3, together with the NUV spectrum of G98. These spectra overlap nicely and cover together the whole range from 1140 to 3200 Å. The combined spectrum offers the possibility to deduce the amount and character-

⁸ <http://www.jb.man.ac.uk/~pulsar/crab.html>.

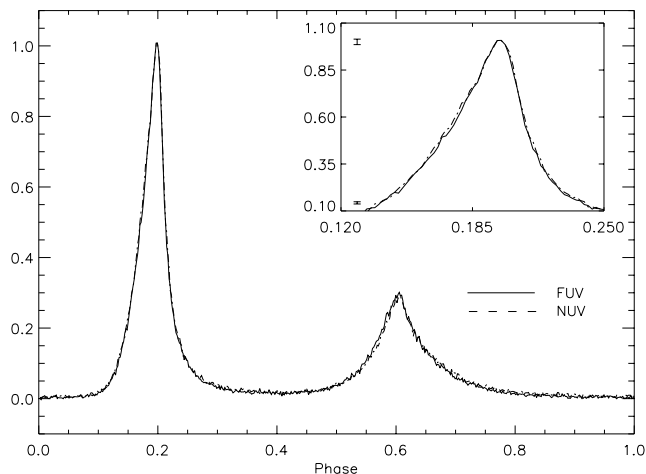


FIG. 2.—Pulse profile of the Crab pulsar in the FUV (solid line). Also shown is the NUV pulse profile from G98 (dashed line). The FUV and NUV data were processed in the same way. The blowup of the primary peak shows the FUV to be slightly narrower. The statistical errors range from 0.003 in the valleys to 0.014 at the peak for both the FUV and NUV profiles, as illustrated by the ($\pm 1 \sigma$) error bars in the insert. Note that the count rate of the pulsar signal is close to zero in the interpulse region.

istics of the interstellar reddening, as well as to determine the dereddened pulsar spectrum itself.

The FUV spectrum was extracted with a 13 pixel wide window. The reductions were made using the CALSTIS

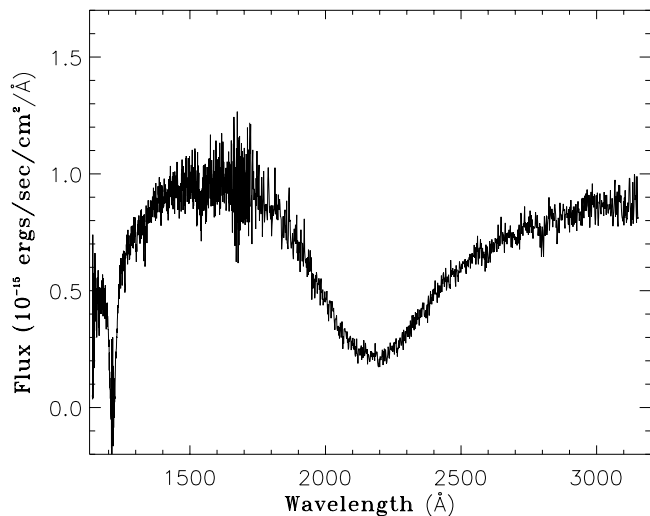


FIG. 3.—Spectrum of the Crab pulsar in the UV. This is a combination of our FUV (1140–1730 Å) observations obtained in 1999 January and the NUV (1600–3200 Å) data from G98. The spectra overlap nicely. The Ly α absorption dip shows some residuals from the subtraction of strong geocoronal emission.

TABLE 2
LOG OF NOT OBSERVATIONS

Grism	Date (1998 Dec)	Wavelength Range (Å)	Resolution (Å)
3.....	24+25	3300–6400	6.6
5.....	24+25	5200–9250	9.0
6.....	27	3200–5500	4.7
7.....	25	3820–6100	5.0
8.....	25	5830–8340	3.6

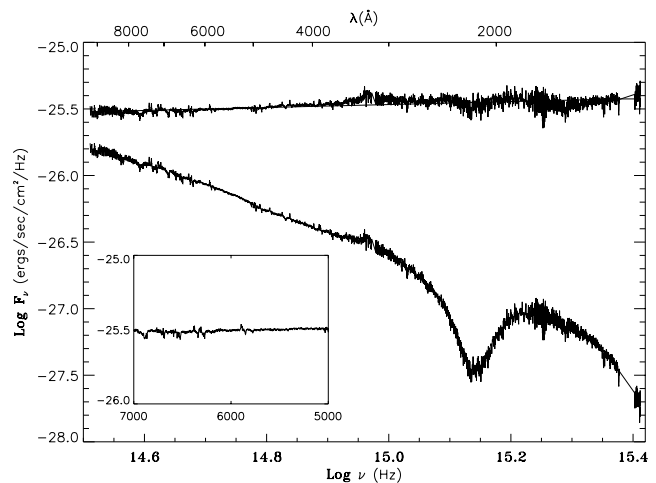


FIG. 4.—Spectrum of the Crab pulsar in the UV and in the optical. The optical data are from NOT. The lower spectrum shows the flux-calibrated spectrum without dereddening. The optical spectrum connects rather well to the NUV data. The uppermost spectrum has been dereddened with $E(B-V) = 0.52$ and $R = 3.1$. The solid line shows the best power-law fit, which has the spectral index $\alpha_\nu = 0.11$. The insert shows a blowup of the optical region where Nasuti et al. (1996) reported a broad absorption dip in the spectrum.

software developed at the GSFC. These IDL routines flat-field the images, and then the point source spectrum is localized and traced on the detector. The extracted pulsar spectrum is background subtracted and converted to absolute flux units using the G140L sensitivity table. The accuracy of the absolute flux calibration is $\sim 15\%$ over the full wavelength scale. Wavelengths are assigned from a library dispersion solution, while the zero-point adjustments are determined from arc frames taken through the 0'05 slit for each science observation. The wavelengths are then converted to heliocentric wavelengths. The accuracy of the wavelength solution is about 0.4 Å.

2.2. Optical Observations

In addition to the UV spectrum, we have also collected data in the optical regime. During several nights in 1998 December we did spectroscopy of the Crab pulsar using the Andalucia Focal Reducer and Spectrograph (ALFOSC) at the 2.56 m NOT on La Palma. In total we obtained 11.25 hr of data in five different grisms. The 1'2 slit was used for all observations (see Table 2 for more details). Not all nights were photometric, and the seeing was generally just above 1". The data were bias-subtracted and flat-fielded. Wavelength calibrations were done using arc frames obtained with a helium lamp. Flux calibration of the spectra was accomplished by comparison to the spectrophotometric standard stars Feige 34 and G191-B2B. To avoid systematic errors due to background subtraction, the slit was put at two different position angles. All observations were made at low air masses and close to the parallactic angle to reduce the effects of atmospheric dispersion; the Crab pulsar passes just 7° from zenith as viewed from La Palma in December. The slit positions for the NOT observations are shown in Figure 1.

2.3. Combined UV/Optical Spectrum

The combined optical and UV observations (both NUV and FUV) are shown in Figure 4. It covers the region 1140–

9250 Å. Although great care was given to the background subtraction of the nebula, the optical spectrum of the Crab pulsar was contaminated by over- and undersubtractions of strong nebular emission lines. These had to be taken out by hand, and we used the IRAF task SPLOT to clean the spectrum interactively. Points that deviated more than 4σ from a smooth continuum fit were rejected. This procedure was robust enough to exclude only clear cases of nebular contamination. The optical spectrum used is a combination of all the different spectra in Table 2. Note that an absolute flux calibration was not applied to the optical spectrum, as the observing conditions were often nonphotometric. Instead we have applied a gray shift to the spectrum to match the *V*-band observations of Percival et al. (1993) and Nasuti et al. (1996). As seen in Figure 4, this is well matched with the UV spectrum from the *HST*.

3. DISCUSSION

3.1. Pulse Profile

The work of Percival et al. (1993) showed small differences in the optical versus NUV pulse profile shapes. They observed the Crab pulsar with the High Speed Photometer (HSP) on board *HST* and found that the main pulse is slightly narrower in the UV than in the optical. Eikenberry et al. (1997) extended the analysis into the near-IR and found that the trend for a decreasing full width half-maximum (FWHM) with decreasing wavelength seems to hold over the full UV-IR range.

The time-tag mode of STIS/FUV-MAMA allows us to examine if the pulse profile of the emission is different in this wavelength region from that in the NUV. The most striking feature of the FUV pulse profile shown in Figure 2 is certainly that it is very similar to the profile previously obtained in the NUV (G98). It appears, however, that the primary peak is slightly narrower in the FUV than in the NUV, as indicated by the blowup of that region in Figure 2. We measured the FWHM of the FUV and NUV primary peak to be 0.0405 and 0.0426 periods, respectively. The position of the peak was determined by a polynomial fit to the central 10 phase bins. The phase at half-maximum was then simply determined by linear interpolation between the two closest phase bins. To estimate a statistical error on the procedure used to measure the FWHM, we computed the FWHM for each of our six FUV observations. The standard deviation obtained in this procedure was 0.001 phase bins. The measured difference in the FWHM of the primary peak can therefore be considered marginally significant. The secondary peak in Figure 2 might actually appear broader in the FUV. It is, however, much noisier than the primary peak, and the same procedure as above could not determine any significant difference to the 13% (3σ) level. The above findings are in agreement with the trend seen in Percival et al. (1993) and Eikenberry et al. (1997). The pulse period obtained from the FUV observations is $P = 33.492675$ ms. Radio data from Jodrell Bank (Lyne et al. 1999) determined the pulse period to be $P = 33.492402$ ms on 1999 January 15. Using their values for the pulse period and its first time derivative on this date we can calculate the period at the time of our *HST* observations. The result is $P = 33.492676$ ms. This agrees with our estimate to seven significant digits. The limiting errors in our computation of the period are the accuracy of the SOLSYS routine, which has a barycentric velocity error of less than

8.0×10^{-7} AU day $^{-1}$ and the unknown accuracy of the rate of the STIS on-board clock.

3.2. The UV Extinction Curve

The phase-averaged UV spectrum of the Crab pulsar must be corrected for a substantial amount of interstellar reddening. The value for $E(B-V)$ has been estimated by a number of authors; Wu (1981) obtained $E(B-V) = 0.50 \pm 0.03$ mag by using the 2200 Å dust absorption feature, the nebular synchrotron continuum, and an extinction curve derived from eight stars. Blair et al. (1992) also used the best fit to the UV nebular continuum and obtained $E(B-V) = 0.51^{+0.04}_{-0.03}$ mag. A different method was used by Miller (1973), who determined the reddening of the Crab Nebula from observations of [S II] lines. Using modern values for the atomic parameters (Keenan et al. 1993; Ramsbottom, Bell, & Stafford 1996), and the extinction curve of Fitzpatrick (1999), his measurements give $E(B-V) = 0.50^{+0.04}_{-0.06}$ mag.

Our data of the pulsar itself allow us to estimate the value for $E(B-V)$ by “ironing out” the 2200 Å bump. To do this we assumed a standard value $R = 3.1$ and dereddened the UV spectrum for different values of $E(B-V)$. The dereddened spectra were then fitted by a power law, and we chose the value for $E(B-V)$ that minimized σ_{α_ν} , the standard deviation of the power-law fit in the region $\log \nu = [14.98, 15.41]$, where the region including the Ly α absorption was excluded. This procedure used the Galactic mean extinction curve from Fitzpatrick (1999) and gave $E(B-V) = 0.52$ mag. This is in excellent agreement with the previous results stated above. As our data have better signal-to-noise ratio and sampling than previous continuum fits, we will use this value as the best estimate of the extinction toward the Crab Nebula throughout this paper.

From the NUV spectrum taken of the Crab pulsar by *IUE*, claims were made for a peculiar extinction curve (Benvenuti et al. 1980). In particular, the 2200 Å bump was reported to be substantially narrower than for the Galactic mean extinction curve, a finding that could indicate that the supernova event itself had altered the grain composition in the Crab Nebula. In principle, both the extinction curve and the intrinsic pulsar spectrum are unknown, which of course makes it troublesome to disentangle these quantities. We take the following approach to this problem: theoretical models favor a power-law spectrum (e.g., Lyne & Graham-Smith 1998) and dereddening with $E(B-V) = 0.52$, $R = 3.1$ indeed gives a power-law pulsar spectrum (Fig. 4), so we will simply assume the intrinsic spectrum of the Crab pulsar to follow a power law $F_\nu = K(\nu/\nu_0)^{\alpha_\nu}$ ergs s $^{-1}$ cm $^{-2}$ Hz $^{-1}$. Here ν is the frequency of the radiation, and K is a constant that is nearly independent of α_ν , when ν_0 is the logarithmic mean frequency of the fitted bandpass (Percival et al. 1993). Using the extinction parameters above, $E(B-V) = 0.52$ and $R = 3.1$, the spectral index is $\alpha_\nu = -0.035$ in the UV range.

By assuming that the intrinsic pulsar spectrum is indeed well represented by the obtained power law, we derived an extinction curve toward the pulsar. This is shown in Figure 5 together with the mean Galactic extinction curve for $R = 3.1$ from Fitzpatrick (1999). The derived extinction curve has a moderately narrower dip (15%) and a somewhat shallower rise in the extreme FUV. Apart from this, it overlaps nicely with the Galactic mean extinction curve. Considering the large variety of measured UV extinction

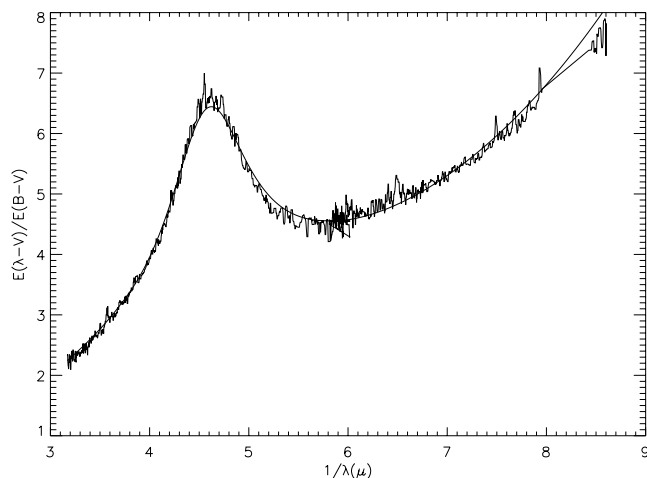


FIG. 5.—UV extinction curve in the direction toward the Crab. This curve was obtained by assuming the pulsar intrinsic spectrum to follow a power law. For comparison, the mean galactic extinction curve from Fitzpatrick (1999) is also shown.

curves (see Fig. 2 in Fitzpatrick 1999), the derived extinction curve toward the Crab can hardly be claimed to be peculiar. Assuming that the pulsar spectrum follows a power law, we conclude that we find no evidence for a nonstandard extinction curve toward the Crab pulsar.

3.3. The Spectral Index of the Pulsar Continuum

According to models, the high-energy pulsar emission, from IR to γ -rays, is produced by (curvature) synchrotron radiation (e.g., Lyne & Graham-Smith 1998, and references therein). A number distribution of electrons following a power law $N(E)dE = CE^{-\gamma}dE$, where E is the energy, C is a constant, and γ is the electron spectral index, will produce synchrotron radiation that has a power-law distribution in flux density $F_\nu = K(\nu/\nu_0)^{\alpha_\nu}$ ergs s⁻¹ cm⁻² Hz⁻¹. The photon spectral index, α_ν , is related to the electron spectral index, γ , via $\alpha_\nu = -(\gamma - 1)/2$ for synchrotron radiation.

The early low-resolution spectroscopy of Oke (1969) appears to peak in the middle of the observed region (~ 3400 – 8000 Å). He reports a slope of $\alpha_\nu = -0.2$ with no stated errors, although he cautions that the uncertainty in the reddening correction could allow also for a positive slope. Much of the theoretical work on the optical emission mechanism of pulsars has been based on this finding (cf. Ginzburg & Zheleznyakov 1975; Lyne & Graham-Smith 1998). More recently, Percival et al. (1993) used ground-based optical broadband photometry together with a NUV photometric point from *HST*/HSP to determine a slope of $\alpha_\nu = 0.11 \pm 0.13$, while Nasuti et al. (1996) obtained a spectrum in the limited wavelength range 4900–7000 Å (see below) and determined $\alpha_\nu = -0.10 \pm 0.01$.

Applying $R = 3.1$ and $E(B-V) = 0.52$ from § 3.2 to our UV spectrum gives a spectral index of $\alpha_\nu = -0.035 \pm 0.040$, where the error is simply the rms around the fit. Obviously, the main uncertainty in this procedure is the extinction parameters. For $E(B-V)$ in the range $[0.48, 0.55]$, the uncertainty due to reddening becomes $\alpha_\nu = -0.035^{+0.094}_{-0.13}$. An accurate estimate of the spectral index obtained in the UV, for the given extinction range, can be obtained by $\alpha_\nu = -0.035 + 3.12[E(B-V) - 0.52]$. Note that the spectral index for $E(B-V) = 0.55$ was erroneously reported in G98. The analysis in this paper supersedes this previous report.

Including the optical spectrum from the NOT gives a wider wavelength range for the fit. The dereddened spectrum shown in Figure 4 was obtained with $R = 3.1$ and $E(B-V) = 0.52$. The best power-law fit to the complete spectrum (excluding Ly α) gives $\alpha_\nu = 0.11$.

Using the full wavelength range we have also tried to constrain both $E(B-V)$ and R . This can be done using the extinction curves from Fitzpatrick (1999), which are a one-parameter family in R . By assuming an intrinsic power law we thus allowed both R and $E(B-V)$ to vary and chose the values that minimized σ_{α_ν} , the standard deviation of the power-law fit. This procedure gives $R = 3.0$ and $E(B-V) = 0.51$, which is consistent with the values used above. In Figure 6 we show the dereddened spectrum of the Crab pulsar for several different values of R and $E(B-V)$. In this figure we have also included IR data from Eikenberry et al. (1997). These plots clearly show the ambiguity of the reddening correction.

We can express the spectral index of the power law fit for the values $E(B-V) = 0.52$ and $R = 3.1$ as $\alpha_\nu = 0.11 \pm 0.04^{+0.21}_{-0.22}$. The first error represents the rms around the power-law fit, and the last errors include all power-law fits in the extinction intervals $R = [2.9, 3.3]$, $E(B-V) = [0.48, 0.55]$. A linear fit, $\alpha_\nu = 0.11 - 0.38(R - 3.1) + 3.88[E(B-V) - 0.52]$, reproduces the obtained α_ν in this interval to better than 0.02 units.

We can only echo Oke (1969) in his conclusion that the uncertainties in reddening corrections are large enough to allow both for negative and positive slopes. The inferred energy distribution for the electrons is given by $\gamma = 0.8 \pm 0.5$. It is worth noting that the only other young pulsar for which a spectrum has been obtained in the optical, PSR B0540–69, had $\alpha_\nu = -1.6 \pm 0.4$ (Hill et al. 1997). This is clearly steeper than the Crab pulsar spectrum.

Finally, the time-tag mode of our FUV observations also allows us to extract phase-resolved spectra, and we have looked for spectral differences during the pulse phase. We found no significant differences above the 5% level, either in the spectrum of the primary versus the secondary peak or in the leading versus trailing part of the primary peak.

3.4. The 5900 Å Feature

In the first report on the optical spectrum of the Crab pulsar, Minkowski (1942) reported a featureless continuum with no absorption or emission lines. The observations of Oke (1969) indicated a similar conclusion, although the spectral resolution was not very good. Since then, few attempts have been made to obtain a better optical spectrum of the Crab pulsar, even though technical development certainly admits improvements. The only modern optical spectrum of the Crab pulsar was obtained with the New Technology Telescope (NTT) by Nasuti et al. (1996). This phase-averaged spectrum covered a rather small wavelength region (4900–7000 Å) and was flat with $\alpha_\nu = -0.10 \pm 0.01$ if dereddened with $E(B-V) = 0.51$. The spectrum was also reported to show a large dip at ~ 5900 Å, the width being ~ 100 Å. According to the authors, this feature probably originates close to the pulsar itself, but no detailed physical mechanism was proposed.

We have searched for this feature in our optical spectra but have found no sign for a dip. This is true for all the different gratings covering this region during all of the nights of data obtained in 1998 December (see Fig. 4). Nor do we see the feature in unpublished data taken by us at

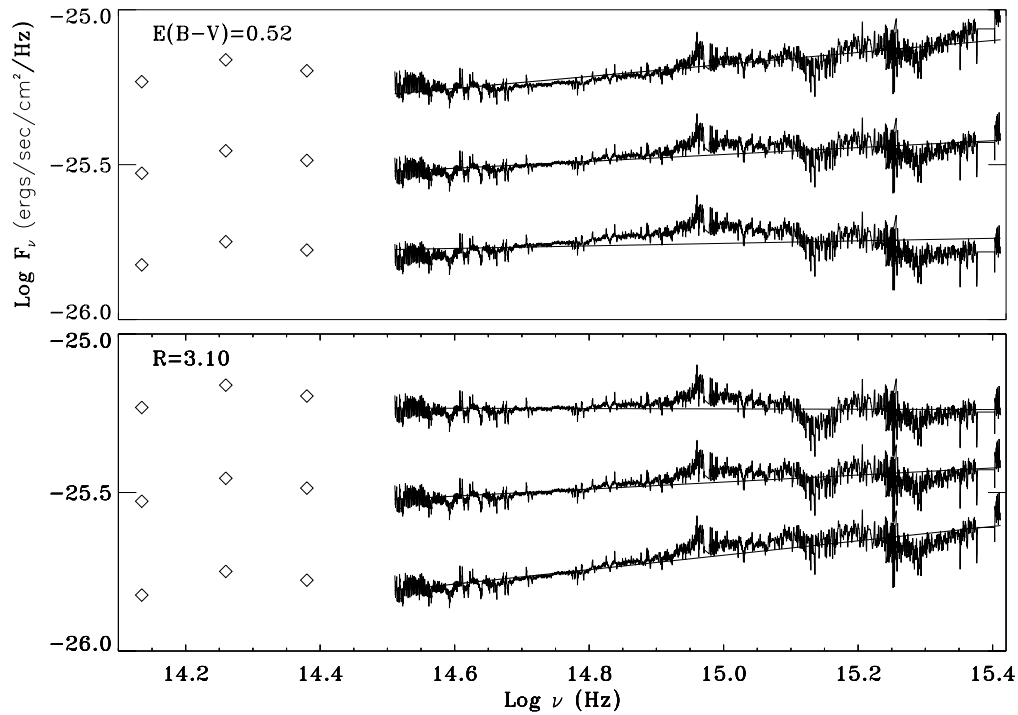


FIG. 6.—Crab pulsar spectrum dereddened with different values of $E(B-V)$ and R . The upper panel shows the dereddened spectrum for $E(B-V) = 0.52$ and three different values of R : 2.9 (upper), 3.1, and 3.3 (lower). The IR data points are from Eikenberry et al. (1997) and are not included in the power-law fits. The fitted power laws have $\alpha_v = 0.19, 0.11$, and 0.041 , respectively. The lower panel shows dereddening for $R = 3.1$ and $E(B-V) = 0.49$ (upper), 0.52 , and 0.55 (lower). The fitted power laws have spectral indices $\alpha_v = -0.005, 0.11$, and 0.23 , respectively. The individual spectra in both panels have been shifted by $-0.3, 0.0$, and $+0.3$ dex in the vertical direction for clarity.

NOT 1 yr earlier (1997 December). Nasuti et al. (1996) noted that the feature became enhanced after flux calibration. This suggests that the dip may be an artifact of the reduction procedure. While their investigation used a single spectrophotometric standard star with flux sampled only every 100 Å, we have used two standard stars with 2 Å sampling in the relevant wavelength region. Although the feature could be time dependent, we propose to regard it as an artifact until confirmed by other observations.

3.5. Absorption Lines

As in the NUV spectrum of the pulsar (G98), the FUV spectrum contains several absorption lines. The identified lines are shown in Figures 7 and 8, and their equivalent widths (EWs) and corresponding column densities, N , are listed in Table 3. For completeness, we have also included the lines in the NUV spectrum identified and measured by G98.

The strongest line is Ly α , and its damping wings can be used to estimate $N(\text{H I})$. To do this we assume that the optical depth in the damping wings is defined by $\sigma(\lambda)N(\text{H I})$ (Shull & Van Steenberg 1985). Here the absorption cross section $\sigma(\lambda) = (4.26 \times 10^{-20} \text{ cm}^2)/(\lambda - \lambda_0)^2$, where the wavelengths are in Å and $\lambda_0 = 1215.67$ Å. We have not considered the instrumental profile, which is much narrower (~ 1 Å) than the line width (see Fig. 7). From this analysis we obtain $N(\text{H I}) = (3.0 \pm 0.5) \times 10^{21} \text{ cm}^{-2}$. The spectrum corrected for Ly α absorption is shown in Figure 7. Our estimated uncertainty in $N(\text{H I})$ reflects the uncertainty in the continuum fit of the corrected spectrum. The column density of free electrons toward the Crab is measured from pulsar dispersion to be $N_e = (0.1755 \pm 0.0007) \times 10^{21}$

cm^{-2} (Comella et al. 1969). The amount of atomic hydrogen is thus $N(\text{H}) = (3.2 \pm 0.5) \times 10^{21} \text{ cm}^{-2}$. This value agrees well with both the result of Schattenburg & Canizares (1986) who obtained $N(\text{H}) = (3.45 \pm 0.42) \times 10^{21} \text{ cm}^{-2}$ from an estimate of the X-ray absorption toward the Crab, and the value we estimate from $E(B-V)$ using the relation in de Boer, Jura, & Shull (1987), which gives $N(\text{H I}) \simeq 3.0 \times 10^{21} \text{ cm}^{-2}$ for $E(B-V) = 0.52$.

The other absorption lines we identify around zero velocity in the FUV spectrum are C I $\lambda\lambda 1277, 1329, 1561, 1658$, C II $\lambda 1335$, O I $\lambda 1303$, Al II $\lambda 1671$, Si II $\lambda\lambda 1260, 1527$, and Si IV $\lambda 1394$. The Si IV line is close to noise level, which

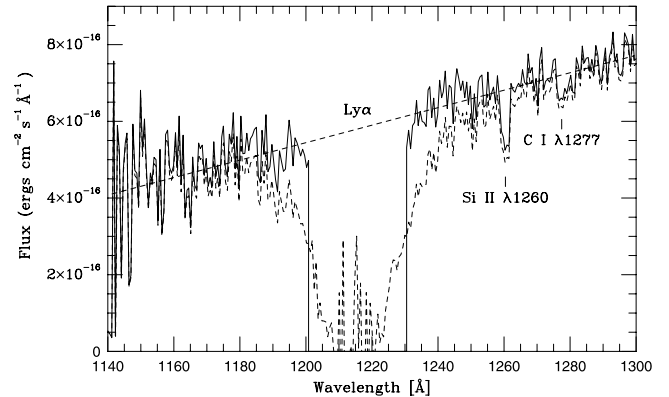


FIG. 7.—FUV spectrum around Ly α . The dashed line shows the original data, and the solid line shows the spectrum after compensation for absorption in the damping wings of Ly α . The column density of neutral hydrogen toward the Crab determined in this way is $N(\text{H I}) = (3.0 \pm 0.5) \times 10^{21} \text{ cm}^{-2}$. The straight dashed line shows a continuum fit to the spectrum after correction for Ly α absorption.

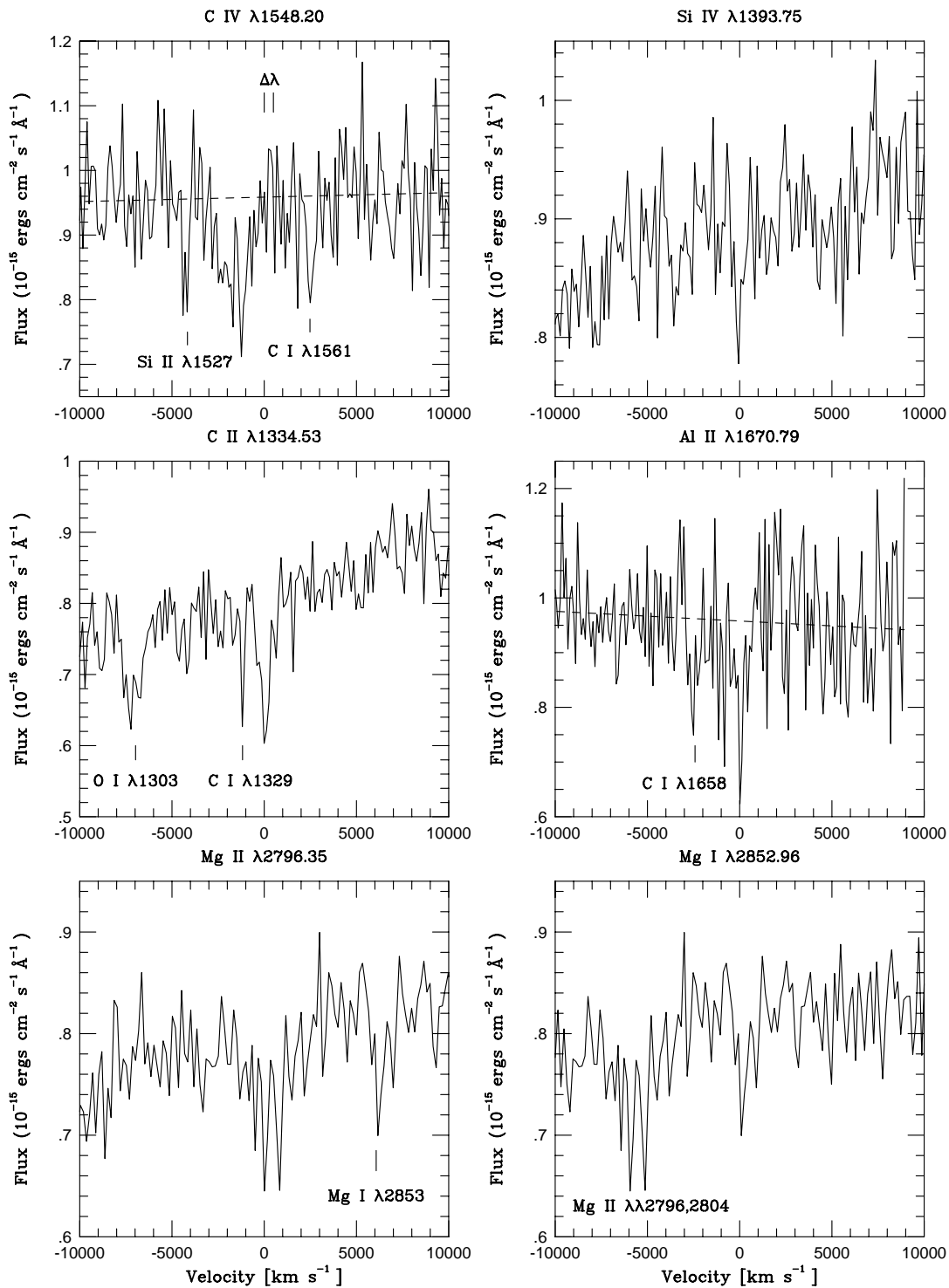


FIG. 8.—Absorption lines seen in the spectrum toward the Crab pulsar. Only C iv $\lambda 1550$ shows absorption that cannot be interstellar (see Fig. 10). The difference in velocity between the two components of the C iv doublet is shown by the two vertical lines marked by “ $\Delta\lambda$.” The equivalent widths of all lines are given in Table 3. Note that the zero velocity of the C ii and C iv multiplets in the figure corresponds to the most blueward component of the multiplets, while Table 3 lists weighted wavelengths.

explains why the Si iv $\lambda 1403$ component is not seen. The C i $\lambda\lambda 1277, 1329$ lines are also marginal detections, but their strengths correspond to those expected when compared with the strengths of C i $\lambda\lambda 1561, 1658$. The C iv $\lambda\lambda 1548, 1551$ doublet is absent at zero velocity but shows a blue-shifted absorption with a maximum shift of $\sim 2500 \text{ km s}^{-1}$. We return to this line in § 3.7.

All lines except Ly α and the C iv doublet, which is not interstellar or from a slow wind (§ 3.7), are unresolved by the moderate spectral resolution in the STIS spectra ($\approx 1.2 \text{ \AA}$ in FUV and $\approx 3.2 \text{ \AA}$ in NUV, corresponding to 250 km s^{-1} and 400 km s^{-1} for the central wavelengths of the two gratings, respectively). The measured EWs of the absorption lines are rather large, which means that we cannot

TABLE 3
ABSORPTION LINES

Species	λ^a (Å)	f_{osc}^a	Equivalent Width (Å)	log (column density) (cm ⁻²)	log (abundance)
H I	1215.67	0.416	37 ± 5	21.48 ± 0.08	12.0
C I	1277.46	0.0966	0.18 ± 0.12	17.49 ± 0.71	7.96 ± 0.76
C I	1329.34	0.0580	0.11 ± 0.11	≤ 18.11	≤ 8.71
C I	1561.05	0.0804	0.35 ± 0.17	18.20 ± 0.46	8.70 ± 0.48
C I	1657.59	0.140	0.54 ± 0.17	17.89 ± 0.29	8.40 ± 0.30
C II	1335.31	0.128	0.46 ± 0.24	18.15 ± 0.50	8.65 ± 0.53
C IV	1549.05	0.286	1.84 ± 0.65	14.45 ± 0.16 ^b	N/A ^b
O I ^c	1303.49	0.0488	0.54 ± 0.21	18.51 ± 0.36	9.02 ± 0.38
Mg I	2852.96	1.830	0.93 ± 0.33	16.11 ± 0.34	6.62 ± 0.35
Mg II	2796.35	0.612	0.79 ± 0.25	16.79 ± 0.28	7.30 ± 0.30
Mg II	2803.53	0.305	0.55 ± 0.27	16.70 ± 0.47	7.20 ± 0.49
Al II	1670.79	1.833	0.56 ± 0.34	16.04 ± 0.57	6.54 ± 0.60
Si II	1260.42	1.007	0.60 ± 0.18	16.82 ± 0.28	7.33 ± 0.29
Si II	1526.71	0.230	0.32 ± 0.14	16.57 ± 0.39	7.08 ± 0.41
Si IV	1393.75	0.514	0.33 ± 0.20	16.63 ± 0.63	7.12 ± 0.66
Fe II	2586.65	0.0646	0.27 ± 0.20	17.15 ± 0.86	7.58 ± 0.96
Fe II	2600.17	0.224	0.40 ± 0.21	16.71 ± 0.53	7.21 ± 0.56

^a Morton 1991.

^b Not interstellar. The column density is calculated from “weak-line” theory (Morton 1991).

^c Could be affected by geocoronal emission and is probably also blended with Si II λ 1304.37

assume that the lines are resolved and optically thin (i.e., we cannot use “weak-line” theory [e.g., Morton 1991]) to derive abundances of the various species, as this would severely underestimate the abundances.

In the absence of a proper model for the distribution of intervening matter, we assume that the absorption is dominated by a single cloud component. We set the intrinsic “Doppler” width in this component to 1 km s⁻¹ and assume that this is the same for all lines. Furthermore, we consider only one spectral component of the lines listed in Table 3. All these assumptions cause us to overestimate the column densities and abundances systematically so that our estimates will be upper limits to these. With this in mind, we calculate Voigt line profiles and EWs as functions of column density, using the atomic data in Morton (1991). From the measured EWs we then obtain column densities and abundances for the interstellar gas toward the Crab. The abundances in Table 3 are presented in the standard logarithmic form, where the value for hydrogen is set to 12.0.

In Table 4, where we have simply co-added the abundances of the different ionization stages of each element, we give the abundances of C, O, Mg, Al, Si, and Fe from our analysis. We also list the solar values for these elements according to Anders & Grevesse (1989). There appears to be

no extreme depletion of any element, contrary to what was stated in G98, where “weak-line” theory was used. This is in agreement with the X-ray observations by Schattenburg & Canizares (1986), which were consistent with a solar abundance of oxygen. Our oxygen abundance from the single O I λ 1303 line is, however, rather uncertain owing to geocoronal airglow corrections and a possible blending with Si II λ 1304. As pointed out above, our method is likely to overestimate abundances systematically. Broader lines, or more cloud components, would lower the abundances derived in accordance with depletion seen in the normal interstellar medium (e.g., 0.65 dex for carbon at 2 kpc; Welty et al. 1999). Spectra with higher resolution are required to refine this analysis.

3.6. Emission Lines

The FUV spectrum contains also information about the Crab Nebula. The long slit covers $\sim 25'' \times 0.5'$ of the nebula, along position angle (PA) 40°5'. The orientation of the slit is shown in Figure 1. To extract the pulsar spectrum we used only 13 of the 1024 pixels of the MAMA detector. To obtain a spectrum of the nebular emission outside this extraction window we again used CALSTIS to produce rectified, wavelength- and flux-calibrated images. As the count rates were very low, we summed the emission from two 8".2 long regions positioned 0".66 above and below the pulsar position. This safely excludes any contribution from the point-spread function (PSF) wings of the pulsar. All emission from all six observations was combined and averaged to increase the signal-to-noise ratio. We present this nebular spectrum in Figure 9, which shows only the wavelength region 1400–1700 Å. This is to exclude the geocoronal lines of Ly α and O I $\lambda\lambda$ 1303, 1356. The spectrum is the average of the regions above and below the pulsar. For the spectrum extracted above (northeast of) the pulsar, the continuum level was flattened artificially. This is because we observed a rising continuum in the red part of this spectrum, which is probably due to contamination of the nearby star seen in Figure 1. Moreover, the count rates in the continuum are

TABLE 4
ABUNDANCES

Element	Solar Value ^a	This Paper ^b
C	8.55	8.9 ± 0.4
O	8.87	9.0 ± 0.4
Mg	7.58	7.4 ± 0.3
Al	6.47	6.5 ± 0.6
Si	7.55	7.6 ± 0.4
Fe	7.51	7.2 ± 0.6

^a Anders & Grevesse 1989.

^b Our method is likely to overestimate the abundances systematically. See § 3.5.

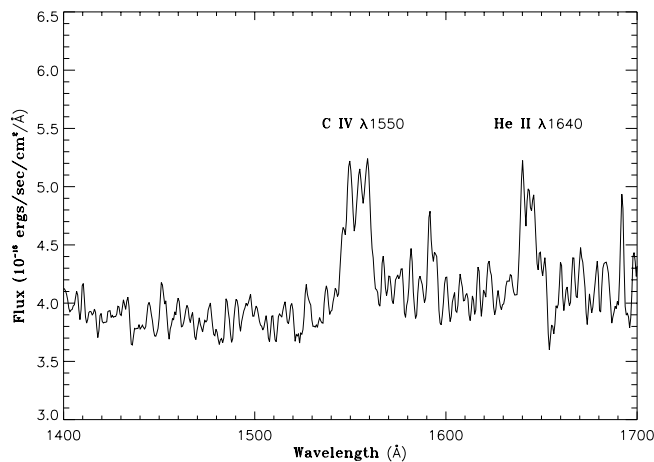


FIG. 9.—FUV emission from the Crab Nebula in the region around the pulsar. The spectrum was obtained by averaging the emission from two $8''.2$ long regions above and below the pulsar position along the $0''.5$ slit. The continuum has been flattened out and the spectrum smoothed with a 3 pixel boxcar average.

only $\sim 7.5 \times 10^{-5}$ counts pixel $^{-1}$ s $^{-1}$. At such low count rates, trends in the dark currents might influence the continuum. No dark images are subtracted from the FUV-MAMA observations because the dark images are known to be variable and to have low count statistics. Therefore, we will not discuss further the slope of the continuum emission from the nebula.

Only two emission lines intrinsic to the Crab Nebula can be seen: C IV $\lambda 1550$ and He II $\lambda 1640$. The measured intensities are $\sim (2.1 \pm 0.8) \times 10^{-15}$ and $\sim (1.4 \pm 0.8) \times 10^{-15}$ ergs s $^{-1}$ cm $^{-2}$, respectively. This is an average for the two $8''.2 \times 0''.5$ regions, just above and below the pulsar. Our detection of these two lines is in accordance with the two previous spectroscopic observations of the Crab Nebula in the FUV. Davidson et al. (1982) used the *IUE* to detect these two lines, as well as C III] $\lambda 1909$. Blair et al. (1992) recalibrated the *IUE* data and complemented these with observations from the Hopkins Ultraviolet Telescope (HUT).

The widths of the lines are approximately 13 and 10 Å, for C IV $\lambda 1550$ and He II $\lambda 1640$, respectively. The width is due to the velocity distribution of the material, the doublet nature of C IV $\lambda 1550$ as well as to the spectral resolution for extended sources for the spectrograph. The bulk of the emission is redshifted by ~ 1000 km s $^{-1}$, although a narrower zero-velocity component is seen from the region above the pulsar.

The flux ratio of C IV $\lambda 1550$ to He II $\lambda 1640$ is thus ~ 1.5 , which is in accordance with the findings of Davidson et al. (1982), who sampled the fluxes over a larger field, $20'' \times 10''$. They used this to argue that the Crab Nebula has no overabundance of carbon. However, the subsequent investigation by Blair et al. (1992) showed that variations in the He II/C IV line ratio exist in the nebula. They cautioned on conclusions regarding the carbon abundance, as differences in physical parameters (e.g., ionization, density, temperature, and clumping) are difficult to disentangle from abundance variations. To determine the carbon abundance is important because it holds the potential to provide information about the ZAMS mass of the progenitor. Comparisons to detailed photoionization models for the large apertures used by *IUE* and *HUT* are hampered by the fact

that ionization conditions are known to change over very small spatial scales (Sankrit et al. 1998). The observations we present have finer spatial resolution and are not biased toward bright filaments. *HST* observations of the same regions in the optical, to establish the ionization conditions, could make more quantitative estimates of the carbon abundance possible.

3.7. The Outer Shell

As was mentioned in § 3.5, and shown in Figure 8, C IV $\lambda 1550$ is the only line in the UV spectrum that shows clear evidence of blueshifted absorption. No evidence for absorption can be seen at zero velocity. The greatest absorption appears to arise in material moving at ~ 1200 km s $^{-1}$ and can thus be due to “normal” Crab Nebula material. However, the absorption seems to continue to higher velocities and can be traced out to ~ 2500 km s $^{-1}$ (see Fig. 10). To estimate the significance of the detection we have calculated an average and rms from two 50 Å regions redward and blueward of the C IV line. Although the line is too noisy for individual pixels to be significant, it consists of many pixels that are consistently below the average. The 11 pixels between 1650 and 2780 km s $^{-1}$ give a detected absorption with a significance of 5.8σ . For the five points in the region 2330–2780 km s $^{-1}$ the significance is 3.0σ .

Together with Clark et al. (1983), who also reported velocities in excess of 2000 km s $^{-1}$, this is the highest velocity ever measured in the Crab and can be interpreted as evidence for the existence of the long-sought fast outer shell (cf. § 1). The column density of C IV in Table 4, $N(\text{C IV}) = (3.0 \pm 1.1) \times 10^{14}$ cm $^{-2}$, assumes the line to be resolved and optically thin. This should be the case for velocity broadening caused by the tentative fast shell, though we caution that the material moving at ~ 1200 km s $^{-1}$ may not be spectrally resolved. The total column density of C IV is therefore likely to be higher, while that of the proposed fast shell is lower than the value given in Table 4. We will now investigate whether the detection is consis-

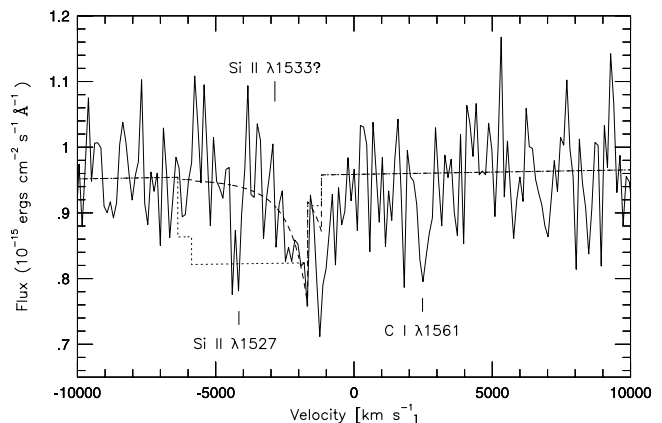


FIG. 10.—Pulsar spectrum around C IV $\lambda 1550$. No absorption at zero velocity of C IV $\lambda 1550$ is seen. Instead the line is blueshifted, reaching a maximum velocity ~ 2500 km s $^{-1}$. The spectrum also shows the interstellar lines Si II $\lambda 1527$ and C I $\lambda 1561$, neither of which blends with the C IV line. Si II $\lambda 1533$, which sometimes accompanies Si II $\lambda 1527$ in interstellar spectra, appears to be absent and cannot explain the observed absorption at velocities $\lesssim 2700$ km s $^{-1}$. Overlaid on the observed spectrum are two of the models for the fast shell in Table 5: $\eta = 0$ (dotted) and $\eta = 3$ (dashed), where η is defined from $\rho(R) = \rho(R_{\text{in}})(R/R_{\text{in}})^{-\eta}$, and R_{in} is the inner radius of the shell. We have assumed that $R_{\text{in}} = 5 \times 10^{18}$ cm, which corresponds to a minimum shell velocity of ~ 1680 km s $^{-1}$. See Table 5 for details of these and other models of the shell.

tent with a fast outer shell model and what information can be provided about the supernova ejecta.

3.7.1. Constraints from C iv $\lambda 1550$

We adopt a model similar to that of LFC86, i.e., outside the observed filaments we attach a massive, freely coasting, spherically symmetric shell. The inner radius, R_{in} , is set to 5.0×10^{18} cm, which agrees with the “mean” inner radius of the presumed shell used by Sankrit & Hester (1997; see their Fig. 7). For free expansion this corresponds to a velocity of ≈ 1680 km s $^{-1}$. Furthermore, we assume that the mass of the shell, M_{sh} , is $4 M_{\odot}$, and that the outer radius of the shell, R_{out} , is 1.9×10^{19} cm. The maximum velocity, V_{out} , is then ≈ 6370 km s $^{-1}$, and the total kinetic energy of the shell, E_{sh} , is 1.0×10^{51} ergs, if the density is constant in the shell. For a density that decreases with radius, E_{sh} is lower, if M_{sh} is held constant. This is shown in Table 5 for density slopes up to $\eta = 9$, where η is defined as $\rho(R) = \rho(R_{\text{in}})(R/R_{\text{in}})^{-\eta}$.

In our model we have used the relative abundances $X(\text{H}):X(\text{He}):X(\text{C}) = 1.0:0.1:3.5 \times 10^{-4}$, where the $X(\text{C})/X(\text{H})$ ratio corresponds to the solar value. With these abundances we have calculated the absorption in C iv $\lambda\lambda 1548, 1551$ as a function of η and the relative fraction of carbon in C iv, $X(\text{C iv})$. The parameter $X(\text{C iv})$ is unity when carbon is all in C iv.

In Figure 10 we show results for two models in which $X(\text{C iv})$ has been kept constant throughout the shell. The dotted line shows the C iv line in the case of $\eta = 0$ and $X(\text{C iv}) = 1$, while the dashed line is for $\eta = 3$ and $X(\text{C iv}) = 0.14$. Both models are described in Table 5. The photoionization models of LFC86 show a case similar to our $\eta = 0$ case (their model 1). There, carbon is ionized beyond C iv, and only a very small fraction, concentrated to the outer edge of the shell, remains in C iv. This gives maximum absorption in the $\eta = 0$ case around -6000 km s $^{-1}$ (see Fig. 1 of LFC86 for such a case). This is clearly not what is seen in the FUV data. On the contrary, the observed absorption peaks at lower velocities, meaning that the C iv number density must be the highest closer to R_{in} . The photoionization models of LFC86 make the $\eta = 0$ case

rather unlikely from this point of view. Instead we turn our attention to steeper density profiles.

Such a situation is highlighted by the $\eta = 3$ case in Figure 10. Our assumption of constant $X(\text{C iv})$ in the shell is probably more realistic for $\eta = 3$ than for $\eta = 0$. This is because the ionization parameter, $\xi = n_{\gamma}/n_e$, where n_{γ} and n_e are number densities of ionizing photons and electrons, respectively, has the radial dependence $\xi \propto R^{\eta-2}$, if absorption can be neglected. With absorption included, η must be greater than 2 to obtain a near-constant $\xi(R)$. Our choice of $X(\text{C iv}) = 0.14$ has been made only to fit the data. Any combination of $X(\text{C iv})$ and M_{sh} , so that $X(\text{C iv})M_{\text{sh}} \approx 0.56 M_{\odot}$, would fit the data equally well. In our model, for $\eta = 3$, this gives a minimum mass [for $X(\text{C iv}) = 1$] of the shell of $M_{\text{sh}} \sim 0.6 M_{\odot}$, and a minimum kinetic energy of $E_{\text{sh}} \sim 8 \times 10^{49}$ ergs.

While a constant $X(\text{C iv})$ in the shell gives a good fit to the line profile for $\eta = 3$, cases with a steeper density dependence must have an ionization structure in which $X(\text{C iv})$ increases outward through the shell. From the radial dependence on the ionization parameter this could be possible but may require a fine tuning between the $R^{\eta-2}$ and $\exp(-\tau)$ parts of ξ . Time-dependent effects are also likely to be important, and the likelihood of an increasing $X(\text{C iv})$ with radius can be explored only by numerical models. We postpone this to a future study. To give the same absorption at 2500 km s $^{-1}$ as the $\eta = 3$ model in Figure 10, models with other η must have $X(\text{C iv}) \sim 1.49^{\eta-3} X(\text{C iv})_{\text{in}}$. The parameter $X(\text{C iv})_{\text{in}}$ is the value of $X(\text{C iv})$ at R_{in} and is the value given in Table 5. For example, for $\eta = 9$, $X(\text{C iv})$ must be ~ 11 times higher at the radius of 2500 km s $^{-1}$ compared to $X(\text{C iv})_{\text{in}}$.

It thus appears as if the observed line profile of the C iv $\lambda 1550$ absorption is consistent with the outer shell being fast and massive. That is, the C iv line cannot exclude that the shell could carry an energy of 10^{51} ergs because the absorption in the gas with the highest velocities (~ 6000 km s $^{-1}$) in the outer shell model would simply disappear in the noise of our rather poor signal-to-noise ratio spectrum.

To limit ourselves to the observed velocities, we adopt a maximum velocity of 3000 km s $^{-1}$ to obtain lower limits on

TABLE 5
PROPERTIES OF A $4 M_{\odot}$ FAST SHELL^a

η^b	$n_{\text{H}}(R_{\text{in}})^b$ ($0.714 \times \rho/\mu_{\text{H}}, \text{cm}^{-3}$)	E_{sh} (10^{51} ergs)	Σ_{Hz}^c (ergs cm $^{-2}$ s $^{-1}$ sr $^{-1}$)	Σ_{Hz}^d (ergs cm $^{-2}$ s $^{-1}$ sr $^{-1}$)	$X(\text{C iv})^e$	M_{trunc}^f (M_{\odot})
0.....	0.12	0.99 (0.03) ^g	$9.3(4.1) \times 10^{-9g}$	$9.2(3.9) \times 10^{-9g}$	1 ^h	0.43
1.....	0.32	0.86 (0.05)	$2.4(1.8) \times 10^{-8}$	$2.1(1.6) \times 10^{-8}$	0.62	0.78
2.....	0.77	0.72 (0.08)	$8.1(7.6) \times 10^{-8}$	$6.1(5.6) \times 10^{-8}$	0.28	1.29
3.....	1.62	0.56 (0.11)	$2.7(2.7) \times 10^{-7}$	$1.7(1.6) \times 10^{-7}$	0.14	1.92
4.....	2.94	0.42 (0.14)	$7.4(7.4) \times 10^{-7}$	$3.8(3.8) \times 10^{-7}$	0.081	2.57
5.....	4.66	0.32 (0.15)	$1.6(1.6) \times 10^{-6}$	$6.9(6.9) \times 10^{-7}$	0.053	3.11
7.....	8.71	0.21 (0.16)	$4.7(4.7) \times 10^{-6}$	$1.4(1.4) \times 10^{-6}$	0.030	3.71
9.....	13.0	0.17 (0.15)	$9.1(9.1) \times 10^{-6}$	$1.8(1.8) \times 10^{-6}$	0.021	3.92

^a Minimum and maximum radii are 5×10^{18} cm and 1.9×10^{19} cm, respectively, corresponding to the velocities ≈ 1680 km s $^{-1}$ and ≈ 6370 km s $^{-1}$.

^b $n_{\text{H}}(R) = n_{\text{H}}(R_{\text{in}})(R/R_{\text{in}})^{-\eta}$.

^c Hz surface brightness at impact parameter $p = R_{\text{in}}$, i.e., just at the edge of the observed nebula $T = 2 \times 10^4$ K).

^d Hz surface brightness at impact parameter $p = 1.1R_{\text{in}}$, i.e., $\sim 17''$ outside the observed nebula ($T = 2 \times 10^4$ K).

^e Fraction of carbon in C iv to obtain the observed optical depth in C iv $\lambda 1550$ at ~ 1680 km s $^{-1}$ [$X(\text{C})/X(\text{H}) = 3.5 \times 10^{-4}$].

^f How much of the $4 M_{\odot}$ shell that resides inside 3000 km s $^{-1}$. Density and $X(\text{C iv})$ at R_{in} are assumed to be the same as for the $4 M_{\odot}$ shell with maximum velocity 6370 km s $^{-1}$.

^g Values in parentheses are for the case with the shell only reaching 3000 km s $^{-1}$, i.e., for the masses in the last column in the table.

^h For $\eta = 0$ the maximum optical depth in C iv $\lambda 1550$ is too small even with $X(\text{C iv}) = 1$ (see Fig. 10).

the mass and energy of the shell. Table 5 shows that M_{sh} could be very low [i.e., $M_{\text{sh}} = M_{\text{trunc}} X(\text{C iv})$, with M_{trunc} defined in Table 5] if η is large and if we only use the absorption at R_{in} as a criterion. However, if we also require that the absorption at 2500 km s^{-1} should be the same for any η as in the $\eta = 3$ model shown in Figure 10, the minimum mass for models with $\eta \geq 3$ is given by $M_{\text{sh}} \gtrsim 1.49^{\eta-3} X(\text{C iv})_{\text{in}} M_{\text{trunc}} M_{\odot}$, which for $\eta = 3$ (4, 5, 7, 9) becomes $M_{\text{sh}} \gtrsim 0.27$ (0.31, 0.37, 0.55, 0.90) M_{\odot} . The kinetic energy corresponding to this M_{sh} (i.e., for $V_{\text{out}} = 3000 \text{ km s}^{-1}$) is $E_{\text{sh}} \gtrsim 1.5$ (1.7, 1.8, 2.4, 3.4) $\times 10^{49}$ ergs. The limits on M_{sh} and E_{sh} for shallower density profiles are fixed by the product $X(\text{C iv}) M_{\text{trunc}}$ (cf. Table 5) and are $M_{\text{sh}} \gtrsim 0.48$ (0.36) M_{\odot} and $E_{\text{sh}} \gtrsim 3.1$ (2.2) $\times 10^{49}$ ergs, respectively, for $\eta = 1$ (2). All these limits scale inversely with the overall abundance of carbon.

To summarize the constraints from C iv $\lambda 1550$, we first emphasize that the line shows that an outer shell with maximum velocity of $V_{\text{out}} \sim 2500 \text{ km s}^{-1}$ appears to be present. We have a $\gtrsim 5 \sigma$ detection of velocities between 1650 and 2780 km s^{-1} . The kinetic energy of the shell depends on its mass, density structure, and extent. For a relatively shallow density profile ($\rho \propto R^{-3}$, or shallower) the kinetic energy of the shell could be as high as 10^{51} ergs, if the shell is spherically symmetric and extends to velocities higher than those we can detect with the obtained signal-to-noise ratio. For a maximum velocity of $\sim 6000 \text{ km s}^{-1}$, the mass of the shell required to obtain this kinetic energy would be 4–8 M_{\odot} . A completely flat density profile, however, seems unlikely from the results of LFC86, both in the fast case (LFC86, model 1), and for a model similar to our $V_{\text{out}} \approx 3000 \text{ km s}^{-1}$ case (LFC86, model 4).

For a density profile steeper than $\rho \propto R^{-3}$ the kinetic energy is most likely less than 10^{51} ergs since the shell mass should be lower than $\sim 8 M_{\odot}$ to be compatible with progenitor models. The lowest mass and energy we estimate for a shell with $V_{\text{out}} = 3000 \text{ km s}^{-1}$ is for $\eta \sim 3$ and are $\sim 0.3 M_{\odot}$ and $\sim 1.5 \times 10^{49}$ ergs, respectively. These values are approximate as they depend on spherical symmetry, the value of R_{in} , and a model fit to the line profile of C iv $\lambda 1548$ at -2500 km s^{-1} , where the line profile is rather uncertain. To distinguish between models with different density slopes (see Table 5), photoionization calculations are needed.

3.7.2. Other Constraints on the Shell

There are, unfortunately, no other lines detected in the UV data that can constrain our current analysis further. Two potentially useful doublets are Si iv $\lambda\lambda 1394, 1403$ and N v $\lambda\lambda 1239, 1243$, but we cannot identify absorption at high velocities in any of these two doublets. The absence of the two doublets is, however, not surprising. Silicon should be more highly ionized than carbon, and LFC86 found that C iv $\lambda 1550$ should produce significantly stronger absorption than N v $\lambda 1240$. The spectral region around N v $\lambda 1240$ is also rather noisy, and the line sits in the damping wing of Ly α . Although the absence of the lines cannot constrain models in this simple analysis, it can be used in conjunction with photoionization calculations to test different models.

The tentative outer shell has been previously searched for also in the optical. Searches in [O III] have been negative for the region outside the observed [O III] skin (cf. Fesen et al. 1997, and references therein). This is not surprising from the point of view of the models of LFC86, in which oxygen is more highly ionized than O III.

A highly ionized massive shell is bound to give rise to H α emission. The deepest search for such emission was done by Fesen et al. (1997) who found a surface brightness limit in H α of $1.5 \times 10^{-7} \text{ ergs cm}^{-2} \text{ s}^{-1} \text{ sr}^{-1}$. With the dereddening suggested by Fesen et al. (1997), i.e., $A_{\text{H}\alpha} = 2.536E(B-V)$, and $E(B-V) = 0.52$ (cf. above), the dereddened surface brightness limit becomes $5.1 \times 10^{-7} \text{ ergs cm}^{-2} \text{ s}^{-1} \text{ sr}^{-1}$. We have calculated the surface brightness in our models to see how it compares with the observed limit. We use a temperature of the tentative shell of $2 \times 10^4 \text{ K}$, which is nearly 3 times higher than that used by Fesen et al. (1997) and Murdin (1994) but is in accordance with the models of LFC86.

The maximum (dereddened) surface brightness in H α , $\Sigma_{\text{H}\alpha}$, occurs at the impact parameter, $p = R_{\text{in}}$, i.e., just at the edge of the observed nebula. The value of $\Sigma_{\text{H}\alpha}$ for this impact parameter is given as a function of η in Table 5 for the model with $M_{\text{sh}} = 4 M_{\odot}$. It is seen that the modeled surface brightness exceeds the observed limit for $\eta \gtrsim 4$. However, $\Sigma_{\text{H}\alpha}$ decreases rapidly with p for large η . Table 5 shows that at $p = 1.1 \times R_{\text{in}}$ (corresponding to $\sim 17''$ outside the observed nebula for a distance of 2 kpc, and roughly where the search by Fesen et al. 1997 was conducted), the surface brightness exceeds the observed limit only for $\eta \gtrsim 5$. For a shell mass as low as 0.3–0.9 M_{\odot} , which we found to be likely lower limits to the shell mass for the density slopes investigated, the shell would easily have escaped detection in H α .

A method to derive parameters for the outer shell was devised by Sankrit & Hester (1997). They estimated the density needed to form a radiative shock at the interface between the nebula and the presumed outer shell, as such a shock is needed in their model to explain the observed [O III] skin. They estimate that a minimum density of $\rho/m_{\text{H}} \sim 12 \text{ cm}^{-3}$ is needed, at least in the presumed equatorial plane of the nebula. If this is true also in the direction toward the pulsar, the models of Sankrit & Hester yield $N(\text{C iv}) \sim 10^{14} \text{ cm}^{-2}$ for the radiative tail of the shock. This would escape detection in our data since the intrinsic line width in their model should be small (much less than our spectral resolution). We can therefore not distinguish between a radiative or adiabatic shock (or no shock at all) in the direction to the pulsar. This also means that it is unlikely that any of the absorption we detect occurs in a region similar to the radiative region in the model of Sankrit & Hester.

Sankrit & Hester (1997) estimate that a mean density at the inner edge of the shell, averaged over all polar angles, should be $\sim 8 \text{ cm}^{-3}$. This would correspond to $n_{\text{H}}(R_{\text{in}}) \approx 5.7 \text{ cm}^{-3}$ for the He/H ratio used in Table 5. To see if we can make a consistent model including the C iv line, the H α surface brightness limit by Fesen et al. (1997), and the model by Sankrit & Hester (1997), we have assumed an upper limit to the shell mass of 8 M_{\odot} (inside $V = 3000 \text{ km s}^{-1}$) and have used the information in Table 5. We then find that $n_{\text{H}}(R_{\text{in}}) \gtrsim 5.7(M_{\text{trunc}}/8 M_{\odot}) \text{ cm}^{-3}$ is required to get a high enough density at R_{in} to agree with the model of Sankrit & Hester (1997). According to the values in Table 5 this is fulfilled for $\eta \gtrsim 3$. The mass and kinetic energy for a shell with such a high $n_{\text{H}}(R_{\text{in}})$ and with $V_{\text{out}} = 3000 \text{ km s}^{-1}$ would be 6.8 (5.0, 3.8, 2.4, 1.7) M_{\odot} and 3.9 (2.7, 1.8, 1.0, 0.7) $\times 10^{50}$ ergs, respectively, for $\eta = 3$ (4, 5, 7, 9). A caveat for this model is that $\Sigma_{\text{H}\alpha}$ at $p = 1.1 \times R_{\text{in}}$ then becomes 2.0 (1.4, 1.0, 0.60, 0.35) $\times 10^{-6} \text{ ergs cm}^{-2} \text{ s}^{-1} \text{ sr}^{-1}$ for $\eta = 3$ (4, 5, 7,

9), which is close to, or higher than, the observed limit. In this scenario, a limit on the $H\alpha$ surface brightness improved by a factor of a few, close to the observed nebula, should be able to distinguish between models with different density slopes even if the He/H ratio is higher than we have assumed. Photoionization models to calculate the temperature accurately and to check the radial dependence on $X(\text{C iv})$ are also needed.

4. CONCLUSIONS

Using STIS on board the *HST* we have observed the Crab Nebula and its pulsar in the far-UV (1140–1720 Å). We have obtained the pulse profile of the pulsar, which is very similar to our previous near-UV profile, although the primary peak appears to be marginally narrower than in the near-UV data (5%, 2 σ). Combining the far- and near-UV data, and assuming an intrinsic power law for the pulsar continuum, we have derived an extinction of $E(B-V) = 0.52$ mag toward the Crab. No evidence for a nonstandard extinction curve was found. We have also added optical spectra taken with the NOT to obtain a spectrum of the pulsar from 1140 to 9250 Å. We have shown that the pulsar spectrum can be well fitted over the full UV/optical range by a power law with spectral index $\alpha_v = 0.11$. The exact value of the spectral index is, however, sensitive to the amount and characteristics of the interstellar reddening, and we have investigated this dependence for a likely range of $E(B-V)$ and R . In the optical, we find no evidence for the dip in the pulsar spectrum around 5900 Å reported by Nasuti et al. (1996).

The interstellar absorption lines detected in the UV have been analyzed and are consistent with normal interstellar abundances. The column density of neutral hydrogen is $(3.0 \pm 0.5) \times 10^{21} \text{ cm}^{-2}$, which corresponds well to the value derived for $E(B-V)$. From the Crab Nebula itself we detect the emission lines C iv $\lambda 1550$ and He II $\lambda 1640$. The ratio of the fluxes of these lines is similar to what has been derived previously, although obtained with much improved spatial resolution.

C iv $\lambda 1550$ is also seen in absorption toward the pulsar. The line is broad and blueshifted with a maximum velocity of $\sim 2500 \text{ km s}^{-1}$, and there is no absorption at zero velocity. These are the highest velocities measured in the Crab and shows that there exists material outside the visible

nebula. This can be interpreted as evidence for the fast shell that has been predicted to surround the Crab Nebula (Chevalier 1977). We have used a simple, spherically symmetric model in which the density in the shell falls off with radius as $R^{-\eta}$ from $5 \times 10^{18} \text{ cm}$ (corresponding to $\approx 1680 \text{ km s}^{-1}$) to derive the mass and energy of such a shell. The conclusions from our model depend on how we tie our model into other observations and models. From the C iv line alone, we find that the minimum mass and kinetic energy of the fast gas are $\sim 0.3 M_\odot$ and $\sim 1.5 \times 10^{49} \text{ ergs}$, respectively. This occurs for a density slope $\eta \sim 3$. A model with a flat ($\eta = 0$) density profile appears unlikely as the required ionization structure disagrees with the modeling of Lundqvist et al. (1986). The maximum mass of the shell is set by progenitor models and is unlikely to be much larger than $8 M_\odot$. With a high shell mass, and the velocity extending to velocities much higher than we can detect, the shell could carry an energy of 10^{51} ergs . The signal-to-noise ratio of C iv $\lambda 1550$ is too low at high velocities to reject or confirm such a conclusion.

Adding constraints from the model of Sankrit & Hester (1997) to those from the C iv line narrows down the parameter space for the shell. In particular, a density slope of $\eta \gtrsim 3$ is required to agree with the interpretation of the observed [O III] skin being a radiative shock. For $\eta \leq 9$, the shell mass is then $\gtrsim 1.7 M_\odot$, and the kinetic energy is $\gtrsim 7 \times 10^{49} \text{ ergs}$. Although the limit on the $H\alpha$ surface brightness from the search of Fesen et al. (1997) tends to favor models with steep density profiles, a model with $\eta = 3$ might still be possible, if the He/H ratio is higher than solar also in the fast shell and the asymmetry of the outer shell is different from that in the model of Sankrit & Hester (1997).

We thank Rob Fesen for help during preparations of the *HST* observations and for discussions and comments on the manuscript. We also thank Phil Plait for help with barycentric corrections and Stefan Larsson for advice on period determination. We thank the Swedish National Space Board, and GSFC/NASA for support which enabled J. S. and P. L. to visit GSFC. We are also grateful to The Swedish Natural Science Research Council for support. J. S. was also supported by grants from the Holmberg, Hierta, and Magn. Bergvall foundations. The research of R. A. C. is supported through grant NAG5-8130.

REFERENCES

- Anders, E., & Grevesse, N. 1989, *Geochim. Cosmochim. Acta*, 53, 197
 Benvenuti, P., et al. 1980, in *Proc. Second European IUE Conference* (ESA SP-157) (Paris: ESA), 339
 Blair, W. P., Long, K. S., Vancura, O., Bowers, C. W., Conger, S., Davidson, A. F., Kriss, G. A., & Henry, R. B. C. 1992, *ApJ*, 399, 611
 Chevalier, R. A. 1977, in *Supernovae*, ed. D. N. Schramm (Dordrecht: Reidel), 53
 Clark, D. H., Murdin, P., Wood, R., Gilmozzi, R., Danziger, J., & Furr, A. W. 1983, *MNRAS*, 204, 415
 Cocke, W. J., Disney, M. J., & Taylor, D. J. 1969, *Nature*, 221, 525
 Comella, J. M., Craft, H. D., Jr., Lovelace, R. V. E., Sutton, J. M., & Tyler, G. I. 1969, *Nature*, 221, 453
 Davidson, K., & Fesen, R. A. 1985, *ARA&A*, 23, 199
 Davidson, K., et al. 1982, *ApJ*, 253, 696
 de Boer, K. S., Jura, M. A., & Shull, J. M. 1987, in *Exploring the Universe with the IUE Satellite*, ed. Y. Kondo, W. Wamsteker, A. Boggess, M. Grewing, C. de Jager, A. L. Lane, J. L. Linsky, & R. Wilson (Dordrecht: Reidel), 485
 Eikenberry, S. S., Fazio, G. G., Ransom, S. M., Middleditch, J., Kristian, J., & Pennypacker, C. R. 1997, *ApJ*, 477, 465
 Fesen, R. A., Shull, M. J., & Hurford, A. P. 1997, *AJ*, 113, 354
 Fitzpatrick, E. L. 1999, *PASP*, 111, 63
 Frail, D. A., Kassim, N. E., Cornwell, T. J., & Goss, W. M. 1995, *ApJ*, 454, L129
 Ginzburg, V. L., & Zheleznyakov, V. V. 1975, *ARA&A*, 13, 511
 Gold, T. 1968, *Nature*, 218, 731
 Gull, T. R., et al. 1998, *ApJ*, 495, L51 (G98)
 Hester, J. J., et al. 1996, *ApJ*, 456, 225
 Hill, R. J., Dolan, J. F., Bless, R. C., Boyd, P. T., Percival, J. W., Taylor, M. J., & Van Citters, G. W. 1997, *ApJ*, 486, L99
 Kaplan, G. H., Hughes, J. A., Seidelmann, P. K., Smith, C. A., & Yallop, B. D. 1989, *AJ*, 97, 1197
 Keenan, F. P., Hibbert, A., Ojha, P. C., & Conlon, E. S. 1993, *Phys. Scr.*, 48, 129
 Kimble, R. A., et al. 1998, *ApJ*, 492, L83
 Lundqvist, P., Fransson, C., & Chevalier, R. A. 1986, *A&A*, 162, L6 (LFC86)
 Lyne, A. G., & Graham-Smith, F. 1998, *Pulsar Astronomy* (Cambridge: Cambridge Univ. Press)
 Lyne, A. G., Pritchard, R. S., & Roberts, M. E. 1999, *Jodrell Bank Crab Pulsar Timing Results Monthly Ephemeris* (Manchester: Univ. Manchester)
 Martin, C., Halpern, J. P., & Schiminovich, D. 1998, *ApJ*, 494, L211
 Mauche, C. W., & Gorenstein, P. 1989, *ApJ*, 336, 843
 Middleditch, J., & Pennypacker, C. 1985, *Nature*, 313, 659
 Miller, J. S. 1973, *ApJ*, 180, L83
 Minkowski, R. 1942, *ApJ*, 96, 199
 Morton, D. C. 1991, *ApJS*, 77, 119

- Murdin, P. 1994, *MNRAS*, 269, 89
- Nasuti, F. P., Mignani, R., Caraveo, P. A., & Bignami, G. F. 1996, *A&A*, 314, 849
- Nomoto, K. 1985, in *The Crab Nebula and Related Supernova Remnants*, ed. M. C. Kafatos & R. B. C. Henry (Cambridge: Cambridge Univ. Press), 97
- Oke, J. B. 1969, *ApJ*, 156, L49
- Percival, J. W., et al. 1993, *ApJ*, 407, 276
- Ramsbottom, C. A., Bell, K. L., & Stafford, R. P. 1996, *At. Data Nucl. Data Tables*, 63, 58
- Reynolds, S. P., & Chevalier, R. A. 1984, *ApJ*, 281, 33
- Sankrit, R., & Hester, J. J. 1997, *ApJ*, 491, 796
- Sankrit, R., et al. 1998, *ApJ*, 504, 344
- Schattenburg, M. L., & Canizares, C. R. 1986, *ApJ*, 301, 759
- Shearer, A., et al. 1997, *ApJ*, 487, L181
- . 1998, *A&A*, 335, L21
- Shull, J. M., & Van Steenberg, M. E. 1985, *ApJ*, 294, 599
- Staelin, D. H., & Reifstein, E. C., III. 1968, *Science*, 162, 1481
- Wallace, P. T., et al. 1977, *Nature*, 266, 692
- Welty, D. E., Frisch, P. C., Sonneborn, G., & York, D. G. 1999, *ApJ*, 512, 636
- Wheeler, J. C. 1978, *ApJ*, 225, 212
- Wu, C. C. 1981, *ApJ*, 245, 581